Mon. Not. R. Astron. Soc. **396,** 2–18 (2009) doi:10.1111/j.1365-2966.2009.14485.x

Gemini/GMOS IFU gas velocity 'tomography' of the narrow line region of nearby active galaxies

F. K. B. Barbosa,[1⋆] T. Storchi-Bergmann,[1] R. Cid Fernandes,[2] C. Winge[3] and H. Schmitt[4,5]

[1]*Instituto de Física – UFRGS, Caixa Postal 15051, CEP 91501-970, Porto Alegre, RS, Brazil*
[2]*Departamento de Física, CFM – UFSC, Campus Universitário – Trindade, CP 476, CEP 88040-900, Florianópolis, SC, Brazil*
[3]*Gemini Observatory, Casilla 603, La Serena, Chile*
[4]*Remote Sensing Division, Code 7210, Naval Research Laboratory, 4555 Overlook Avenue, SW, Washington D.C. 20375, USA*
[5]*Interferometric Inc., 13454 Sunrise Valley, Suite 240, Herndon, VA 20171, USA*

Accepted 2009 January 9. Received 2008 December 17; in original form 2008 September 3

ABSTRACT

We present two-dimensional (2D) mapping of the gas velocity field of the inner few hundred parsecs of six nearby active galaxies, using spectra obtained with the integral field unit of the Gemini Multi-Object Spectrograph instrument at the Gemini North telescope. In our previous paper, we reported the 2D mapping of the stellar kinematics extracted from the calcium triplet absorption lines. In this paper, we use the [S III] λ9069 emission line to obtain the flux distribution and kinematics of the gas in the narrow-line region (NLR). The gas emission is extended by a few hundred parsecs and its kinematics are dominated by rotation in the galaxy plane. Subtraction of the rotation component reveals outflows along the NLR which show spatial correlation with radio structures seen in Very Large Array radio 3.6 and 20 cm flux images, suggesting that the radio jet is pushing the circumnuclear interstellar medium. This interpretation is also supported by the observation of high-velocity dispersion ($\sigma \geq 500\,\mathrm{km\,s^{-1}}$) structures in association with the outflowing gas. The gas outflows and radio jets are oriented at random angles relative to the galaxy major axis, indicating that they are not launched perpendicularly to the galaxy plane. Slicing the emission-line profiles into velocity channels, we create maps of the NLR gas distribution at different radial velocities. In at least half of our sample, the highest velocities are observed close to the nucleus suggesting that the emitting gas is decelerating outwards, from projected blueshifts exceeding $400\,\mathrm{km\,s^{-1}}$ to values of 100–200 $\mathrm{km\,s^{-1}}$ at 100–200 pc from the nucleus. We have estimated mass outflow rates in the NLR of ≈1 to 50 × $10^{-3}\,\mathrm{M_\odot\,yr^{-1}}$, which are ≈10–20 times the accretion rate necessary to feed the active nucleus. The kinetic energy of the ouflow is estimated to be 4–5 orders of magnitude smaller than the bolometric luminosity. Assuming kinetic energy transfer between the radio jet and the NLR outflows, the mass ejection rate in the radio jet is 5–6 orders of magnitude smaller than the mass accretion rate necessary to feed the nuclear supermassive black hole.

Key words: galaxies: active – galaxies: kinematics and dynamics– galaxies: nuclei – galaxies: Seyfert.

1 INTRODUCTION

The narrow-line region (NLR) of active galactic nuclei (AGNs) is an important laboratory to probe the interaction between the nuclear engine and the circumnuclear interstellar medium (ISM) of the host galaxies. In the recent past, narrow-band imaging of the NLR in optical emission lines has been used to determine the properties of the radiation field of the AGN (Schmitt & Kinney 1996; Ferruit, Wilson & Mulchaey 2000). Long-slit spectroscopic studies have been used to provide the missing kinematics and spectral information (e.g. Storchi-Bergmann, Wiklson & Baldwin 1992; Storchi-Bergmann et al. 1999; Cooke et al. 2000; Fraquelli, Storchi-Bergmann & Binette 2000; Ruiz et al. 2001; González Delgado et al. 2002; Fraquelli, Storchi-Bergmann & Levenson 2003).

⋆E-mail: faustokb@if.ufrgs.br

Comparison of optical observations with data in other wavebands can provide clues on the origin of the NLR excitation and kinematics. Ground-based observations of Seyfert galaxies with large extended NLRs have shown that there is a good correlation between the orientation of the [O III] emission and that of the radio jet (Wilson & Tsvetanov 1994; Nagar et al. 1999). These results have been confirmed by observations with the *Hubble Space Telescope* (*HST*) (Capetti et al. 1996; Falcke, Wilson & Simpson 1998; Schmitt et al. 2003). Combining this information with the fact that Seyfert galaxies with luminous radio sources have systematically broader [O III] emission lines (Whittle 1992) indicates that the NLR gas can be significantly disturbed by the interaction with the jet. This interaction can either ionize the gas through shocks or simply compress it, resulting in regions of enhanced emission and outflows.

In some active galaxies, however, the interaction of the radio jet with the ISM is less important. Using *HST* STIS spectra, Nelson et al. (2000) studied the NLR kinematics and emission-line ratios of NGC 4151 and concluded that there is no significant interaction of the radio jet with the galaxy ISM. Mundell et al. (2003) proposed that the misalignment of the NLR and the radio jet in NGC 4151 favours photoionization by the AGN as the main excitation mechanism of the NLR. Also using Space Telescope Imaging Spectrograph (STIS) spectra, Das et al. (2006) studied the NLR of NGC 1068 and concluded that the radio jet is not the principal driving force on the outflowing NLR clouds.

Veilleux et al. (2003) used the Taurus Tunable Filter on the Anglo-Australian Telescope (AAT) and William Herschel Telescope to search for very extended ionized gas in starburst and active galaxies and confronted their data with optical long-slit spectra and X-ray maps and concluded the source of ionization in the gas ranges from shock ionization to photoionization by the central AGN or by in situ hot young stars. New powerful observational tools to study the NLR are the integral field units (IFUs) as they allow for both spatial and spectroscopic coverage (Allington-Smith et al. 2002; Riffel et al. 2006; Dumas et al. 2007; Riffel et al. 2008).

In this work, we have used the Gemini Multi-Object Spectrograph (GMOS) in IFU mode to map the NLR distribution and kinematics of six Seyfert galaxies using the [S III]λ9069 emission line. Due to the relatively high-spectral resolution of our data we were able to slice the emission-line profiles in a sequence of velocity channels, allowing for the mapping of different velocity components from the blue to the red wing of the [S III] emission line. We also compare the gas kinematics and distribution with radio 20- and 3.6-cm maps in order to evaluate the role of the radio jet in the imprint of the NLR kinematics. Finally, we compare the NLR kinematics with the stellar one – obtained from the calcium triplet around 8500 Å – already published in Barbosa et al. (2006; hereafter Paper I) what has alowed the separatation of the contribution of the gravitational component – namely rotation in the galactic plane – from outflows along the NLR.

This paper is organized as follows. In Section 2, we present the selected galaxy sample and their most relevant information and discuss briefly the observations and reduction steps. In Section 3, we describe the data analysis methods and in Section 4 we report our results. In Section 5, we discuss and interpret our results and in Section 6 we present a summary and our conclusions.

2 SAMPLE, OBSERVATIONS AND REDUCTIONS

The sample consists of six nearby Seyfert 1 and Seyfert 2 galaxies for which we have studied the stellar kinematics in Paper I. The galaxies and their main properties are listed in Table 1 together with the seeing of the corresponding observation. The observation log is given in Paper I and a summary of the observations is given below.

Table 1. Sample galaxies (column 1), morphological/Seyfert type (columns 2/3), adopted spatial scale (column 4) and seeing measured from the acquisition images (columns 5/6).

Galaxy	Morph. type[a]	Seyfert type	Scale (pc arcsec^{-2})	Image quality[b] (arcsec)	(pc)
NGC 2273	SB(r)a	2	120	1.00	120
NGC 3227	SAB(s) pec	1.5	84	0.80	67
NGC 3516	(R)SB(s)0	1.5	183	0.98	180
NGC 4051	SAB(rs)bc	1	45	0.50	23
NGC 4593	(R)SB(rs)b	1	174	0.49	85
NGC 4941	(R)SAB(r)ab	2	72	0.40	29

[a]Morphological type as given in NED (NASA/IPAC Extragalactic Data base http://nedwww.ipac.caltech.edu/).
[b]Although this has been obtained from the PSF measured in the acquisition image, we verified that the nuclear PSF measured in the reconstructed image of the Seyfert 1 galaxies is the same for NGC 4051 and only ∼10 per cent larger in NGC 4593.

2.1 IFU data

The galaxies were observed in three runs at the Gemini North telescope with the GMOS spectrograph operating in IFU mode. The spectral range was similar for the three runs, always including the calcium triplet absorptions at ≈λ8500 Å and the [S III]λ9069 Å emission line, with spectral resolution $R \sim 3000$ (FWHM ∼ 100 km s^{-1}) and wavelength sampling of 0.692 Å pixel^{-1}. The GMOS IFU consists of a hexagonal array of 1000 lenslets which sends the light through optical fibers to the spectrograph. The lenslet array samples a field of view (FOV) of 7×5 arcsec^2 (or half of it, 3.5×5 arcsec^2, with twice the wavelength coverage). The sky is sampled with a set of lenses which is displaced by 1 arcmin from the object and whose field is half the object field. The centres of contiguous lenses are separated by 0.2 arcsec and thus the distance between opposite faces of the hexagonal lenses is also 0.2 arcsec. A more complete discussion on the IFU instrument and the observational details can be found in Paper I.

Data reduction was accomplished using generic IRAF[1] tasks and specific ones developed for GMOS data in the GEMINI.GMOS package. The reduction steps consisted of trimming, bias subtraction, flat-fielding, cosmic rays cleaning, alignment and interpolation of the data, extraction of the spectra, wavelength and flux calibration, sky-subtraction and coaddition of different exposures.

2.2 Radio data

High-resolution VLA[2] radio images were fetched from the VLA archive and reduced or were kindly provided by the authors of previously published works (Nagar et al. 1999; Schmitt et al. 2001). The data from Nagar et al. (1999) have been recently reprocessed

[1] IRAF is distributed by the National Optical Astronomy Observatories, which is operated by the Association of Universities for Research in Astronomy, Inc. (AURA) under cooperative agreement with the National Science Foundation.
[2] The Very Large Array (VLA) is a facility of the National Radio Astronomy Observatory, which is operated by Associated Universities, Inc. under a cooperative agreement with the National Science Foundation.

Table 2. Radio observations.

Name	Program/ Ref.	Date	Conf.	Wavelength (cm)	Beam size (arcsec)	Beam PA (°)
NGC 2273	AM 384[a]	1993 January 16	A	3.6	0.29 × 0.29	0
	AU 79	1999 August 29	A	20	1.44 × 1.22	2.0
NGC 3227	AP 212	1991 June 24	A	3.6	0.38 × 0.29	9.4
	AU 79	1999 August 29	A	20	1.66 × 1.28	-43.8
NGC 3516	AM 384[a]	1993 January 18	A	3.6	0.32 × 0.32	0
NGC 3516	AM 384	1993 January 18	A	20	1.68 × 1.12	20.2
NGC 4051	AP 212	1991 June 24	A	3.6	0.32 × 0.26	36.4
	AU 79	1999 August 29	A	20	1.85 × 1.10	-84.5
NGC 4941	AA 394[b]	1993 January 18	A	3.6	0.35 × 0.24	37.2

[a]Published in Nagar et al. (1999).
[b]Published in Schmitt et al. (2001).

for better flux calibration than those originally published. We list in Table 2 the VLA program from which the observations were obtained or the reference to the work where they were published, the date of the observations, the array configuration, wavelength of the observation and the beam parameters used for the image restoration. The reductions followed standard AIPS techniques, which consisted of flagging bad data points, setting the flux-density scale using the primary calibrators and phase calibrating using the secondary calibrators. Images were created using natural weighting and were also interactively self-calibrated two times in phase.

3 DATA ANALYSIS

As the surface brightness of the galaxies decreases towards the borders of the field, the signal-to-noise ratio of the spectra decreases accordingly. To compensate for this effect, we have replaced each individual spectrum by the average of itself and the six nearest spectra (inside a radius 0.3 arcsec). This replacement was done for the spectra beyond a radius 1 arcsec from the centroid of the λ8500 Å continuum brightness distribution. By adopting this strategy to increase the signal-to-noise ratio we lose some spatial resolution at the borders of the field but as the smoothing aperture is of the order of the seeing, this effect is not important.

3.1 Line fluxes, peak velocities and widths

In order to obtain the [S III] integrated line fluxes the original hexagonally sampled spectral array was interpolated into a rectangularly sampled 0.1×0.1 arcsec^2 spectral array (data cube). The data cube was then integrated over the wavelength range covering the full spectral extent of the line and the continuum was removed by subtracting its contribution under the line using an interpolation of the flux between two adjacent continuum windows, one to each side of the [S III] line.

The radial velocities and the velocity dispersions have been measured directly in the original hexagonally sampled array by fitting Gaussians to the [S III] emission line. This fit was done with the FITPROFS task in two steps. In the first step the task was run with fixed Gaussian width and free peak wavelength and flux. By doing this, we obtain a robust determination of the peak wavelength, from which we calculate the radial velocity. In order to compare the gas radial velocities with the stellar ones from Paper I we have corrected the measured radial velocities to the local standard of rest (LSR).

In order to obtain the emission-line widths (full width at half-maximum, FWHM), we run the FITPROFS task again with fixed peak wavelength. The instrumental spectral broadening, obtained measuring the widths of the calibration lamp emission lines, was finally taken into account by subtracting it, in quadrature, from the [S III] line widths. From the line widths we have then obtained the gas velocity dispersions $\sigma = \mathrm{FWHM}/2.355$.

3.2 Velocity 'tomography'

We have obtained a 'velocity tomography' in the [S III] emission lines slicing its profile into velocity channels and integrating the flux of the line within each velocity channel. The flux images in the velocity channels were constructed in a similar way to that used to create the integrated line flux image. The rectangularly interpolated data cube was sliced into small wavelength ranges of ∼1.4 Å (2 pixel or ∼46 km s^{-1}) to create each channel image. The number of channels depends on the width of the emission line for each galaxy, spanning the full wavelength range of the [S III] line in each galaxy. The adjacent continua images used to remove the continuum from each channel are the same ones used to remove the continuum of the integrated [S III] line flux image.

As we gain an extra dimension with the IFU technique we must be careful in the analysis of the wealth of information gained. The velocity channel maps provide different information from that of the radial velocity maps. The latter gives the peak velocity of the emission line for a given spatial position and it is dependent on the relative intensities of different kinematic components eventually present to form an emission line. The peak emission will usually correspond to the kinematics of the component(s) with the highest flux(es). The velocity channel maps, however, show how the gas with a certain velocity is distributed along the NLR. For example: a blueshifted jet can be seen in a high-velocity channel and the radial velocity map can show a low velocity (or even redshifted velocity) in that same location if the low-velocity (or redshifted) gas has a much higher flux than that of the jet.

4 RESULTS

2D maps of the [S III] kinematics are presented for each galaxy in pairs of figures from Figs 1, 2 to 11, 12. The first figure of each pair comprises six panels, as described below.

(1) The top-left hand panel shows the [S III] emission-line integrated flux.

(2) The top-right hand panel shows the continuum integrated in a spectral window of 470 Å centred in the CaT spectral region.

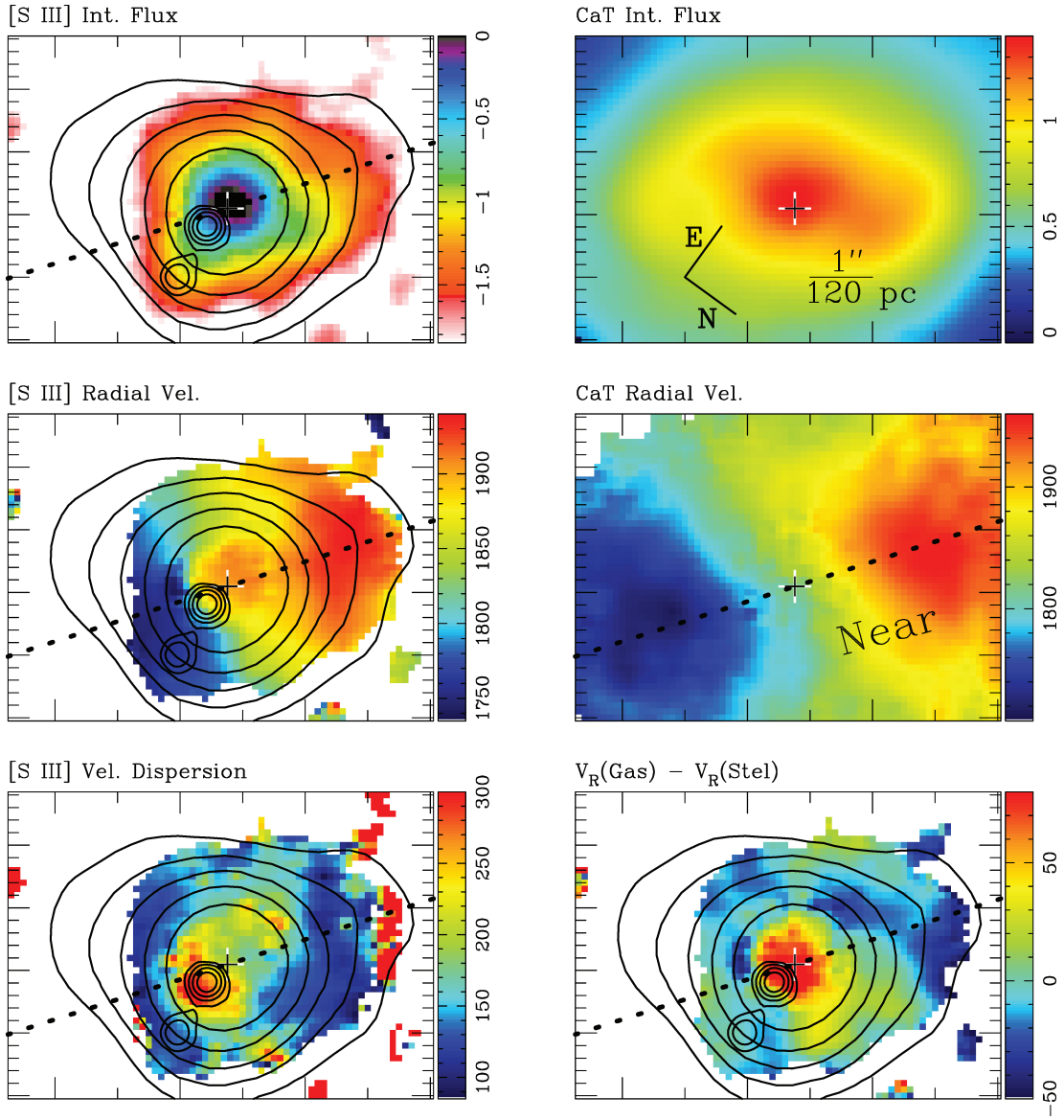

Figure 1. Gas kinematics of NGC 2273. The black contours in the four gas maps are radio 3.6 (compact contours) and 20 cm maps. The upper-left hand panel shows the integrated [S III] line flux. The central-left hand panel shows the [S III] radial velocity map. The bottom-left hand panel shows the [S III] velocity dispersion map. The bottom-right hand panel shows the difference between the [S III] and stellar radial velocities. The central-right hand panel shows the stellar radial velocity map. The upper-right hand panel shows the continuum flux integrated over 470 Å at the CaT spectral region. The colour bars of the panels showing flux measurements are in logarithm of arbitrary flux units and those showing velocity measurements are in km s^{-1} units. The systemic velocity for this galaxy is 1836 km s^{-1} (Barbosa et al. 2006). All panels have the same orientation, indicated at the upper-right hand panel. The panels have all the same scale, indicated in the upper-right hand panel, and dimensions of 6.8 × 4.9 $arcsec^2$. Tick marks in the *x*-axis are separated by 1 arcsec, as well as the large ones in the *y*-axis. Regions in white correspond to uncertain measurements which were masked out. The dashed line shows the orientation of the line of nodes from Paper I and the word 'Near' indicates the near side of the galactic plane.

(3) The middle-left hand panel shows the [S III] radial velocity field.

(4) The middle-right hand panel shows the stellar radial velocity field from Paper I.

(5) The bottom-left hand panel shows the [S III] velocity dispersion map.

(6) The bottom-right hand panel shows the difference between the [S III] and stellar radial velocity maps.

In all panels the stellar kinematical centre is identified by the black cross. Radio contours have been overlaid on the [S III] maps as described in each figure caption. Unless otherwise specified the alignment of the maps was done registering the maxima of the radio and [S III] flux distributions. Panels 2 and 4 are included for comparison purposes only.

The second figure for each galaxy presents the velocity tomography along the [S III] emission-line profile. Radio contours, as in the previous figure, were also overlaid on one of the maps. The number of channels shown depends on the width of the emission line but each image always corresponds to a velocity width of 46 km s^{-1}.

We now discuss the results for each galaxy.

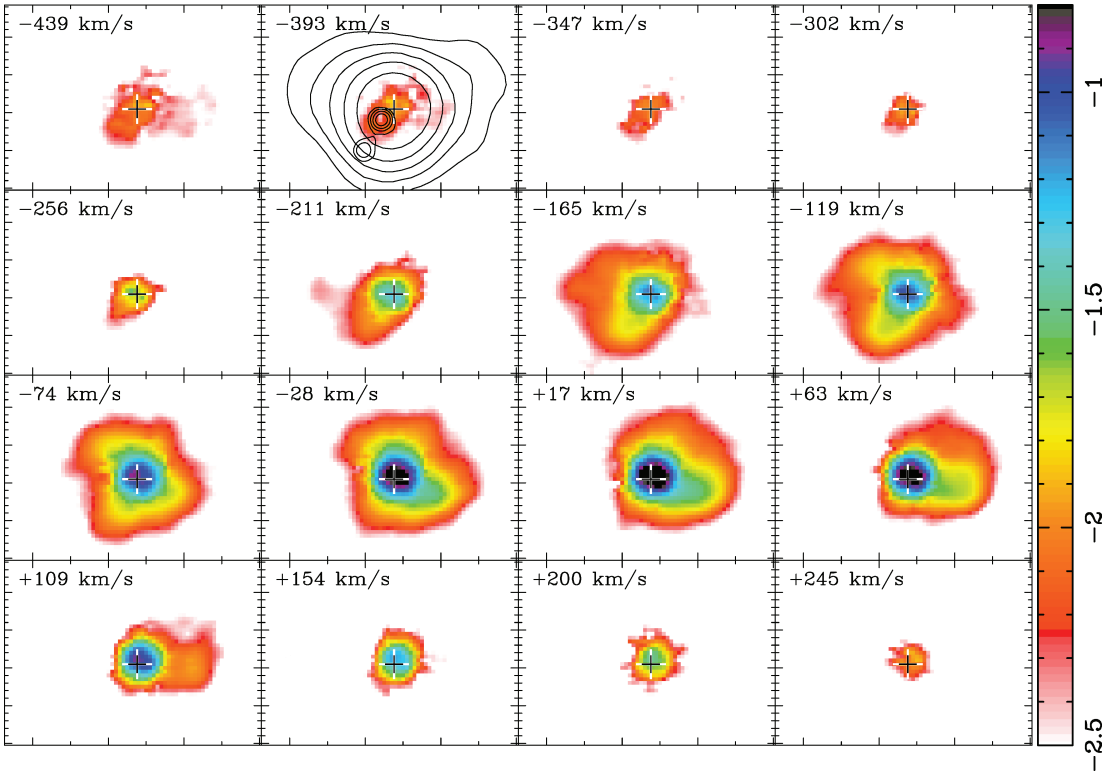

Figure 2. NGC 2273 velocity slices along the [S III] emission-line profile. The slices have a ∼46 km s^{-1} width and the central velocity is given in the upper-left hand corner. Radio contours, as in the previous figure, were overlaid on the map corresponding to the velocity channel −393 km s^{-1}. The size of each slice field is 6.8 × 4.9 arcsec^2 and the orientation is the same of the previous figure. Tick marks in the *x*-axis are separated by 1 arcsec, as well as the large ones in the *y*-axis.

4.1 NGC 2273

The map of the [S III] integrated flux (upper-left hand panel of Fig. 1) shows a bright central peak and resolved extended emission by as much as ∼3.5 arcsec to NE. The overlaid radio 3.6-cm contours (inner ones) is composed of two discrete components: the strongest at ∼0.6 arcsec and the another ∼1.5 arcsec to the W. This radio image was registered to the peak of our [S III] emission map by using the nuclear position adopted by Nagar et al. (1999) in their radio image.

Comparison of the [S III]-integrated flux with fluxes in the 16 velocity channels of Fig. 2 suggests the presence of at least four kinematic components. The first kinematic component is observed as a linear structure extending to W by ≤1 arcsec from the nucleus. This structure is cospatial with the strongest 3.6 cm radio component to the W and it is also observed in the most blueshifted channels (−439 to −347 km s^{-1}). The second kinematic component is approximately cospatial with the second radio component at ∼1.5 arcsec W, and is observed from channels −211 to −74 km s^{-1}. A third kinematic component is observed extending from the nucleus up to ∼2 arcsec to S–SW in velocity channels from −211 to −74 km s^{-1} and a fourth component is observed from channel −28 to 109 km s^{-1} extending up to ∼2 arcsec to N–NE. These two latter kinematic components could be associated with the nuclear spiral arms observed by Erwin & Sparke (2003). Another component may be present in channels from −74 to 63 km s^{-1} extending towards E by ∼1.5 arcsec.

Except for a central redshifted region, the [S III] radial velocity map (middle-left hand panel of Fig. 1) keeps a good resemblance to the stellar one with the line of nodes along NE–SW. In the difference map [V_R(Gas) − V_R(Stel]; lower-right hand panel of Fig. 1) the [S III] velocity residuals are within the range −50 to +50 km s^{-1} but for the redshifted region within the inner 0.5 arcsec which have redshifts in excess of 50 km s^{-1}.

The [S III] σ map (bottom-left hand panel of Fig. 1) shows a strong increase (from ∼100 to ∼300 km s^{-1}) in the velocity dispersion values within 1 arcsec W of the nucleus. This high σ region is cospatial with the strongest 3.6 cm radio component and with the highest blueshifted component observed in the velocity channel maps. This result is consistent with a model in which a small radio jet interacts with the circumnuclear ISM producing the blueshifted [S III] emission. Towards the E, there is also a hint of enhancement of the σ values, which could be associated with a counterjet, which is hard to observe due to the fact that it is probably behind the galaxy disc.

These opposite outflows are oriented approximately along E–W (position angle PA ∼90°), while the kinematic major axis of the central region (from Paper I) is at PA = 53° (see dashed line in Fig. 1). Under the assumption that the spiral arms are trailing in this galaxy, the near side of the galaxy is projected to the NW and the far side to the SE as shown in the middle-right hand panel of Fig. 1. The blueshifted outflows are thus projected on to the near side of the galaxy. Using the disc inclination angle from Paper I as $i = 50°$ we infer that the outflows are launched at a small angle $\theta < 40°$ with respect to the galaxy disc, what could explain the increase in σ associated with the radio component closer to the nucleus: due to the small angle, the radio plasma compresses the gas from the disc, while the gas corresponding to the second component has already left the disc.

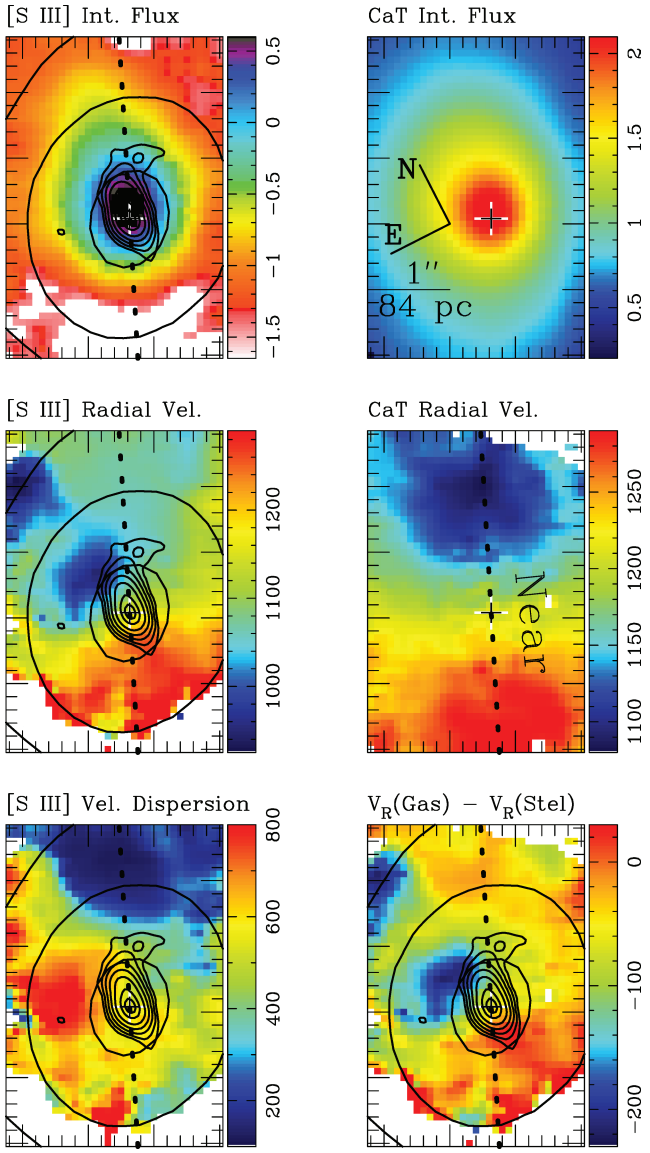

Figure 3. Gas kinematics of NGC 3227. Details are as described in the caption of Fig. 1, except that the IFU field is half the size, or 3.3×4.9 arcsec^2. The large tick marks in the x-axis are separated by 1 arcsec, as well as those in the y-axis. The systemic velocity for this galaxy is 1201 km s^{-1} (Barbosa et al. 2006).

4.2 NGC 3227

The [S III] integrated flux map (upper-left hand panel of Fig. 3) shows extended emission in all directions but the flux drops more abruptly towards S and SE and extends beyond the field boundaries towards W, N and E. Inside the field boundaries the strongest emission is clearly more elongated towards N along PA $\sim -5^\circ$.

The radio 20 cm (outer contours) is extended beyond the field-of-view and presents no structure at the scale of our maps. The radio 3.6 cm (inner contours) is compact but resolved being more elongated to N suggestive of a compact radio jet which has the same orientation of the strongest [S III] emission.

Comparison of the integrated flux with the flux in velocity channels (Fig. 4) shows a compact kinematic component elongated to the N with very high blueshifts of up to ~ -900 km s^{-1} close to the nucleus (within $\sim$1 arcsec). More extended emission to the N is observed in the channels ~ -465 to -7 km s^{-1}. This emission has a changing orientation from PA $\sim 10^\circ$ to PA $\sim -10^\circ$ and increasing extent as we move from the most blueshifted to the zero-velocity channels, suggesting the ejected mass interacts with the ISM and changes its orientation and decelerates with distance from the nucleus.

The radial velocity field (middle-left hand panel of Fig. 3) shows two conspicuous blueshifted regions to the N, approximately in the direction of the compact radio structure but lying just beyond it, at distances of 0.7 and 2.4 arcsecs from the nucleus ($\approx$60 and 200 pc projected distance at the galaxy, respectively). These blueshifted regions are also visible in the difference map [V_R(Gas) − V_R(Stel); lower-right hand panel of Fig. 3] and have velocities relative to the stellar velocity field of about -200 km s^{-1} and could be regions of the ISM of the galaxy compressed by the radio jet observed at 3.6 cm. A comparison between the radial velocity field and difference map with the high blueshifts observed within 1 arcsec from the nucleus in the velocity channels (Fig. 4) of up to -900 km s^{-1} suggests that we are observing the creation of a new optical emitting gas structure, probably due to the interaction of the compact radio ejecta observed in the 3.6 cm radio image with the circumnuclear gas.

The σ map (bottom-left hand panel of Fig. 3) shows a wide range of σ values from $\sim$100 km s^{-1} at N to $\sim$800 km s^{-1} at NE. The regions with the highest σ values are located just eastwards of the two blueshifted emission regions, suggesting that this enhancement is due to compression of the galaxy ISM by the outflowing radio ejecta.

The outflows are observed at PA $\sim 10^\circ$, while the kinematic major axis of the central region is at PA $= -30^\circ$ (Paper I). Under the assumption that the spiral arms are again trailing, the near side of the galaxy is projected to the W–SW (as shown in the middle-right hand panel of Fig. 3) and the far side is the E–NE, thus the blueshifted outflows are projected against the far side of the galaxy.

4.3 NGC 3516

The [S III] integrated flux map (upper-left hand panel of Fig. 5) shows nuclear emission elongated towards the north along PA $\sim 20^\circ$ and connected to a region of enhanced emission (hereafter N cloud) at $\sim$2 arcsec which seems to extend beyond the field boundaries.

The radio 20 cm emission shows a clear spatial association to the [S III] emission being also elongated towards N being cospatial to the region of the N cloud. This radio emission was first observed by Miyaji, Wilson & Perez-Fournon (1992) who refer to it as 'radio cloud B'. These authors also pointed out the coincidence between this cloud and a peak in an [O III]λ5007 image, suggesting compression and acceleration of ambient gas of the galaxy by radio ejecta from the active nucleus.

The maps of flux in velocity channels (Fig. 6) clearly reveal blueshifts in the N cloud in the channels from -357 to -128 km s^{-1} at 2 arcsec N from the nucleus. A possible opposite velocity (redshifted) component to the S is partially visible from channel $+9$ to $+147$ km s^{-1} extending beyond the IFU field. The gas at the nucleus also presents significant blueshift – up to -311 km s^{-1}, while the highest redshift there is $\sim$190 km s^{-1}.

Both the radial velocity field (middle-left hand panel of Fig. 5) and the difference field (bottom-right hand panel of Fig. 5) deviate significantly from the stellar velocity field (middle-right hand panel

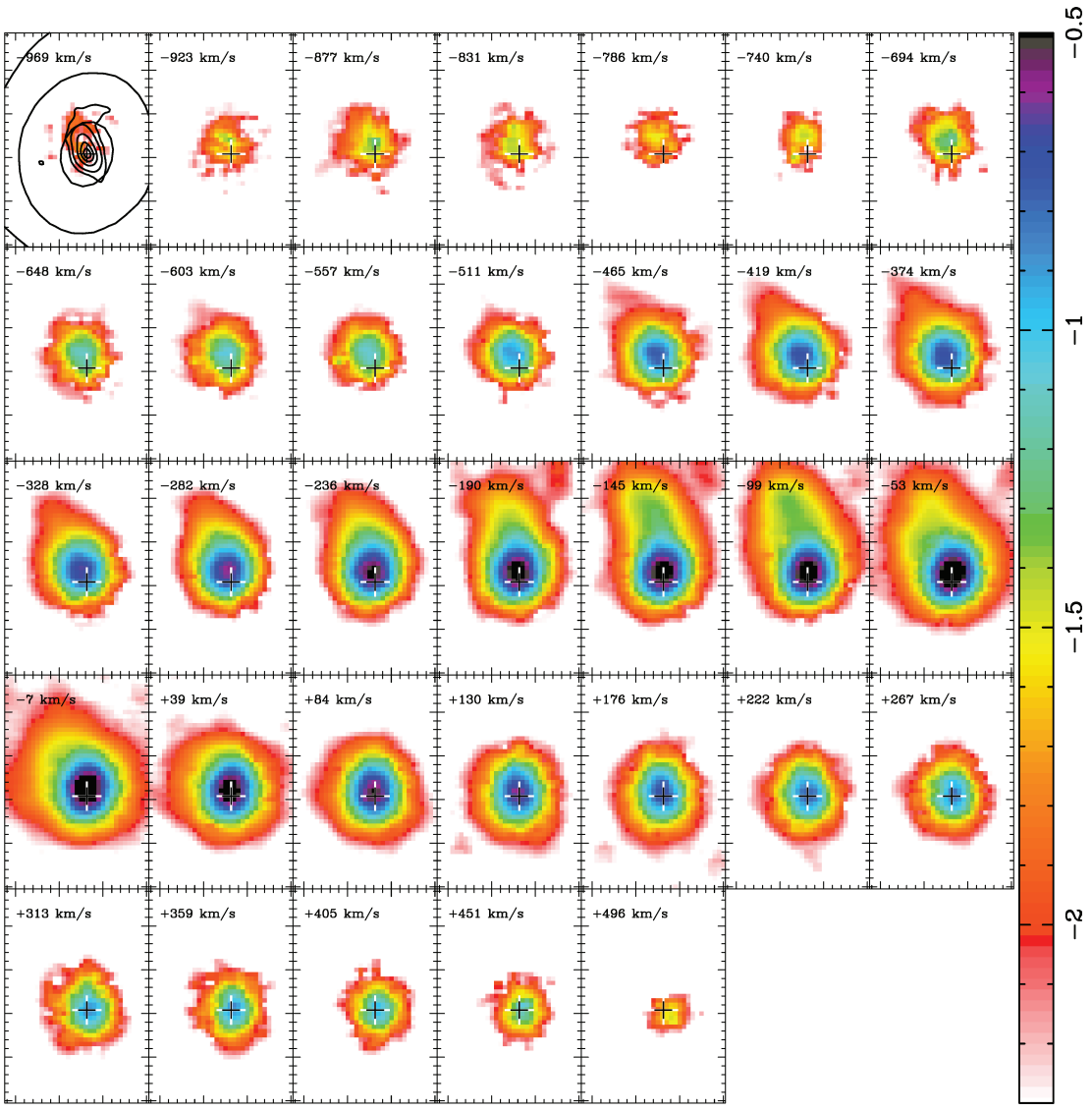

Figure 4. NGC 3227 velocity slices along the [S III] emission-line profile. The slices have a ∼46 km s^{-1} width and the central velocity is given in the upper-left hand corner. Radio contours, as in the previous figure, were overlaid on the upper-left hand map. The size of each slice field is 3.3 × 4.9 arcsec^2 and the large tick marks in the *x*-axis are separated by 1 arcsec, as well as the ones in the *y*-axis.

of the Fig. 5) at the position of the N cloud which is blueshifted by ∼ −200 km s^{-1} in accordance with what was found in the velocity channels.

Mulchaey et al. (1992) have studied the kinematics of the extended Hα and [N II] emitting gas in NGC 3516 using long-slit spectroscopy over the inner 15 arcsec (thus covering a larger field than ours), finding a significant rotational component but also radial components of motion. They propose a model of a bipolar mass outflow in which gas ejected from the nucleus out of the plane of the stellar disc is slowed by gravitational forces and falls back into the plane (beyond 5 arcsec from the nucleus). More recently, Ruiz et al. (2005) obtained slitless *HST* STIS spectra and reached a similar conclusion from the kinematics of the [O III] λ5007 emitting gas. They observe blueshifts which reach ≈ −200 to −300 km s^{-1} at ∼2 arcsec N of the nucleus, similarly to what we observe in the [S III] emitting gas. Beyond 2 arcsec N the blueshifts decrease reaching the sistemic velocity at ∼6 arcsec, supporting the ejection model of Mulchaey et al. (1992). Our observations also support the ejection model, although we only observe the inner part of the jet that is coming out of the plane towards the N.

The σ map (bottom-left hand panel of Fig. 5) shows a narrow arc with high σ which seems to delineate the borders of the blueshifted N cloud. The high σ structure indicates perturbations in the surrounding interstellar medium which supports the interpretation first put forth by Miyaji et al. (1992) of compression of the galaxy ISM by the outflowing radio ejecta.

The stellar kinematic major axis of the inner region, as derived in Paper I, is at PA = 48°, while the blueshifted N cloud is at PA ∼ 20°. Under the assumption that the spiral structure is trailing, the near side of the galaxy is the NW (as shown in the middle-right hand panel of Fig. 5), thus the N cloud is seen projected against the near side of the galaxy. Using the disc inclination angle from Paper I as $i = 22°$ we infer that the outflows form an angle $\theta < 68°$ with the galaxy disc.

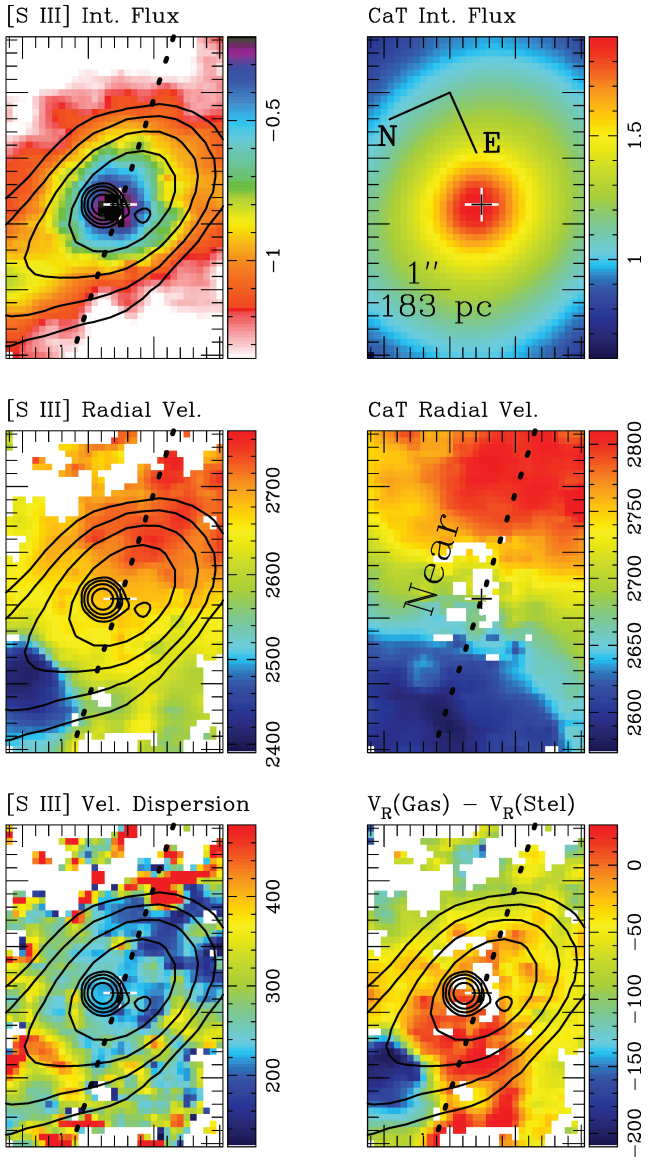

Figure 5. Gas kinematics of NGC 3516. Details are as described in the caption of Fig. 1, except that the IFU field is half the size, or 3.3×4.9 arcsec^2. The large tick marks in the x-axis are separated by 1 arcsec, as well as the ones in the y-axis. The systemic velocity for this galaxy is 2698 km s^{-1} (Barbosa et al. 2006).

4.4 NGC 4051

The [S III] integrated flux map (upper-left hand panel of Fig. 7) shows a complex emission structure. The strongest emission is centred at the nucleus and is elongated by ∼5 arcsec from W to E. At low flux levels, the emission reaches ∼3 arcsec from the nucleus to the S and ∼4 arcsec to N and NE.

The thin contours in Fig. 7 show the 20-cm radio distribution, which is elongated to the S–SW where there is a 'secondary' or fainter 'peak' at ∼3 arcsec from the nucleus. The strongest radio source at 20 cm is centred at the nucleus and is elongated from W to E, and is well traced by the strongest [S III] emission. The thicker contours in Fig. 7 show the 3.6 cm radio contours which are elongated by only ∼1 arcsec to W and E, and have the same orientation as that of the strongest radio source at 20 cm and of the [S III] strongest emission.

The velocity slices (Fig. 8) show four kinematic components. The most extended component is a thin filament to the N up to the border of the field with blueshifts in the range −498 to −315 km s^{-1}. The second most extended component is observed to the E, up to 2 arcsec from the nucleus with blueshifts of −315 to −40 km s^{-1}. A component to the S is seen from channel −40 to +52 km s^{-1} and thus presents no significant net radial velocity. A component to the W is visible in channels with velocities ranging from +97 to +281 km s^{-1} and seems to be a counterpart to the E component, although presenting smaller redshifts than the blueshifts observed to the E. A NE emission patch is present with modest redshift in channels with velocities −40 to +97 km s^{-1} at 2.5 arcsec from the nucleus.

The radial velocity map (middle-left hand panel of Fig. 7) as well as the difference map (bottom-right hand panel of Fig. 7) shows a bi-polar E–W component reaching velocities of ≈ +100 and −250 km s^{-1} with respect to the stellar radial velocity field at ≈2 arcsec from the nucleus. This bi-polar component has the same orientation as the compact 3.6 cm radio structure, suggesting that it is an outflow related to this radio emission. But while the radio emission is restricted to at most 1 arcsec from the nucleus, the outflows observed in [S III] extend farther beyond, up to 2.5 arcsec from the nucleus to the E. The blueshifts observed to the E indicate that this side of the outflow is partially directed towards us and the fact that the blueshifts have higher velocities than the redshifts suggest that the redshifted outflow is partially hidden behind the galaxy disc. A very high-velocity blueshift, of up to −400 km s^{-1}, is observed at ≈2 arcsec to the N, and corresponds to the filament with the highest blueshifs observed in the velocity channels maps. The orientation of this high-velocity filament is approximately perpendicular to the direction of the compact E–W radio structure and to the E–W outflow.

The σ map (bottom-left hand panel of Fig. 7) shows a wide range of velocity dispersion values, which vary from some tenths of km s^{-1} up to ∼10^3 km s^{-1}. The highest σ values are associated to the tip of the blueshifted outflow to the E and to the highest blueshift to the N. There are other two regions with σ as high as 400 km s^{-1} at the locations covered by the bipolar component, at ∼2 arcsec E and ∼1 arcsec W of the nucleus. This association again support that the origin of the high σ values is the injection of kinetic energy into the circumnuclear gas as a result of the interaction of a radio jet with the ISM of the host galaxy.

The stellar kinematic major axis of the nuclear region obtained in Paper I is PA = 107°, while the outflows are observed to the E and N (blueshifts) and W (redshifts). Under the assumption that the spiral arms are trailing, the near side of the galaxy is the SW and the far side is the NE (as shown in the middle-right hand panel of Fig. 7), thus the two blueshifted components are projected against the far side of the galaxy (in front of the galactic disc) and the redshifted component is behind the galactic disc.

4.5 NGC 4593

The integrated flux map (upper-left hand panel in Fig. 9) presents extended emission by ∼5 arcsec from SE to NW and by ∼3 arcsec in the perpendicular direction. The strongest emission is elongated from the nucleus to the W along PA ∼ 280° extending to ≈2 arcsec from the nucleus.

The radio map of this galaxy is not resolved and only shows a compact nuclear component (Schmitt et al. 2001).

The velocity channels in Fig. 10 shows a range of velocities from −203 to +207 km s^{-1}, with the highest values at the nucleus.

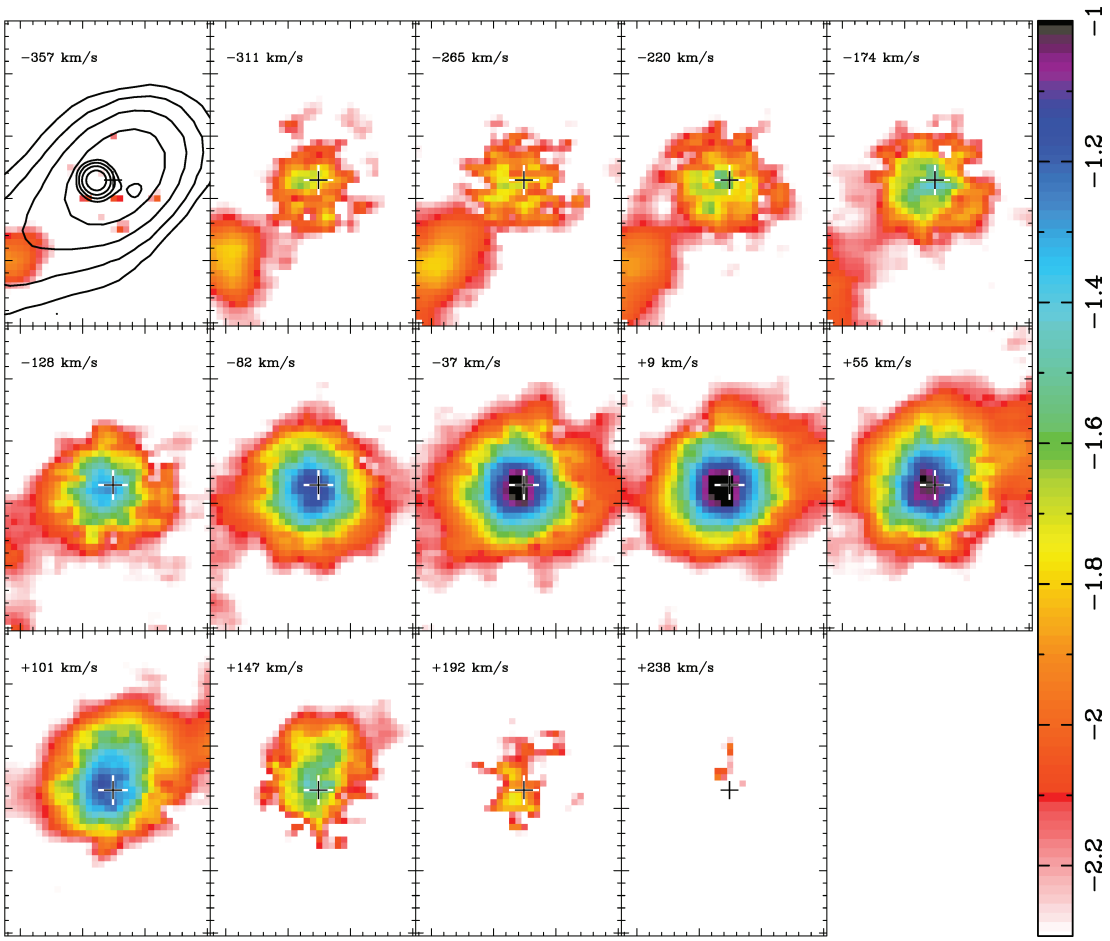

Figure 6. NGC 3516 velocity slices along the [S III] emission-line profile. The slices have a ∼46 km s^{-1} width and the central velocity is given in the upper-left hand corner. Radio contours, as in the previous figure, were overlaid on the upper-left hand map. The size of each slice field is 3.3 × 4.9 arcsec^2 and the large tick marks in the *x*-axis are separated by 1 arcsec, as well as the ones in the *y*-axis.

The elongation to the W is observed in the channels ∼ −100 to +100 km s^{-1}, suggesting it comprises both blueshifts and redshifts. Nevertheless, in the [S III] radial velocity map (middle-left hand panel of Fig. 9) it can be observed that the gas shows a rotation pattern similar to that of the stars, except at the end of the elongated structure at ∼2 arcsec W of the nucleus. In the stellar radial velocity map, it can be observed that the rotation velocity at this location is approximately +100 km s^{-1}, thus similar to the redshift observed in the velocity channels for the elongated structure. It can thus be concluded that the redshifted emission observed in the velocity channels probably originates from gas rotating in the plane while the blueshifted emission is due to gas coming out of the plane. The residual blueshift is also observed in the difference map V_R(Gas) − V_R(Stel), which shows blueshifts in excess of 50 km s^{-1}.

At the location where the residual blueshift is observed, we find a conspicuous region of low velocity dispersion values in the σ map (bottom-left hand panel of Fig. 9) which seems to be detached from the rest of the region, which shows much higher σ values. The low σ values suggest that this region may be a high-latitude cloud outflowing from the nuclear region without interaction with the circumnuclear ISM, unlike the other outflows discussed previously in which shocks produced by the interaction of the radio ejecta with the circumnuclear ISM of the galaxy can explain the observed enhancement of the σ in the outflowing region.

The stellar kinematic major axis of the nuclear region from Paper I is at PA = 89° (or 269°), while the outflowing region is observed at PA ∼ 280°. Under the assumption that the spiral arms are trailing, the near side of the galaxy is the N and the far side is the S (as shown in the middle-right hand panel of Fig. 9), and the blueshifted region is thus projected against the near side of the galaxy.

4.6 NGC 4941

The [S III] integrated flux map (upper-left hand panel of Fig. 11) is extended by ∼3.5 arcsec in all directions and presents a faint patch of emission towards S which extends beyond the border of the field (2.2 arcsec S from the nucleus).

The contours of the 3.6 cm radio emission shown in Fig. 11 shows a small extent (by ≤1 arcsec) to NW.

In the velocity slices maps (Fig. 12) there is no conspicuous features, except that the highest blueshifts (more than −400 km s^{-1}) seem to occur at the location of the small radio extension to NW suggesting the presence of a compact outflow. The highest redshifts (more than 300 km s^{-1}) are observed in the opposite direction, suggesting a possible counterpart outflow not seen in the radio map.

The radial velocity map (middle-left hand panel of Fig. 11) does not show an obvious rotation pattern, as observed in all other galaxies. The difference map (bottom-right hand panel of Fig. 11) show

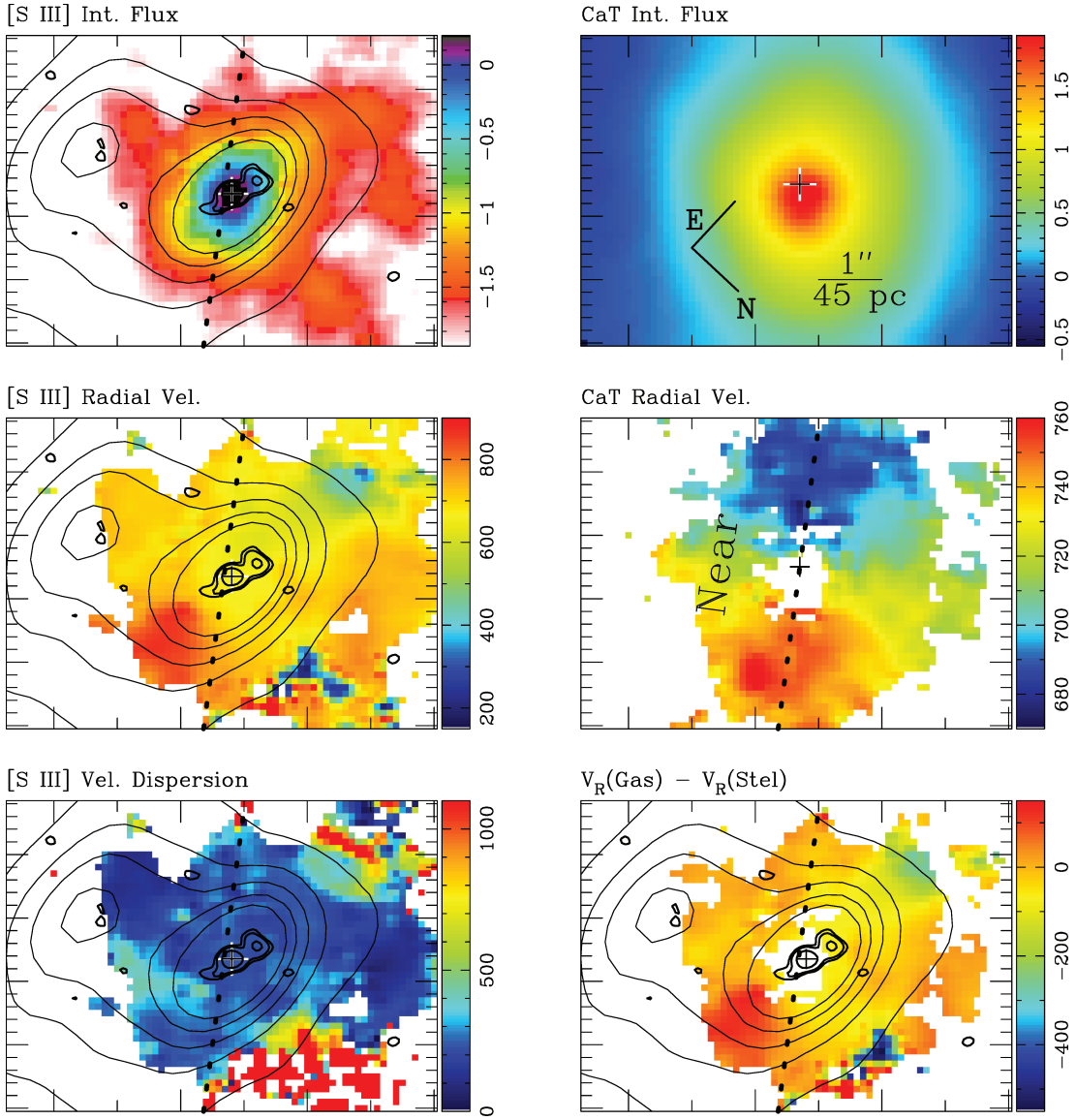

Figure 7. Gas kinematics of NGC 4051. Details are as described in the caption of Fig. 1. The systemic velocity for this galaxy is 718 km s^{-1} (Barbosa et al. 2006).

redshifts to the NE ($50 < V_R < 100$ km s^{-1}) and similar blueshifts to the SW which suggests a mild outflow along SW–NE.

The stellar kinematic major axis of the nuclear region is at PA = 20° (Paper I, errata), while the blueshifted part of the possible compact outflow associated to the radio jet has an average PA ∼ −40° and the mild outflow is observed at PA ∼ 35°. Under the assumption that the spiral arms are trailing the near side of the galaxy is the E (as shown in the middle-right hand panel of Fig. 11) and the blueshifted part of both the compact and most extended outflows are projected against the far side of the galaxy.

5 DISCUSSION

5.1 [S III] flux distribution

The [S III] emission is extended by several arcseconds in all six galaxies of our sample, corresponding at the galaxies to radial distances from the nucleus ranging from ≈150 pc in NGC 4941, through typical values for most galaxies of ≈250 pc to a radial distance larger than 400 pc in NGC 3516.

For the five galaxies with resolved radio maps (NGC 2273, 3227, 3516, 4051 and 4941) the gas emission is enhanced in regions where the radio emission is detected and the outflows are observed. Nevertheless the emission is not restricted to these regions but is spread over most of the IFU field and in two cases extending beyond the field. From its kinematics it can be concluded that this emission originates in gas rotating in the disc of the galaxy. The ionizing source of this gas could be the AGN and/or eventual circumnuclear star formation in the galaxy disc.

5.2 Gas kinematics

The [S III] radial velocity field shows a conspicuous rotation pattern similar to that of the stars in NGC 2273, 3227, 3516 and 4593. But, besides rotation, we have found additional kinematic components at locations usually associated to radio components, corresponding mostly to outflows.

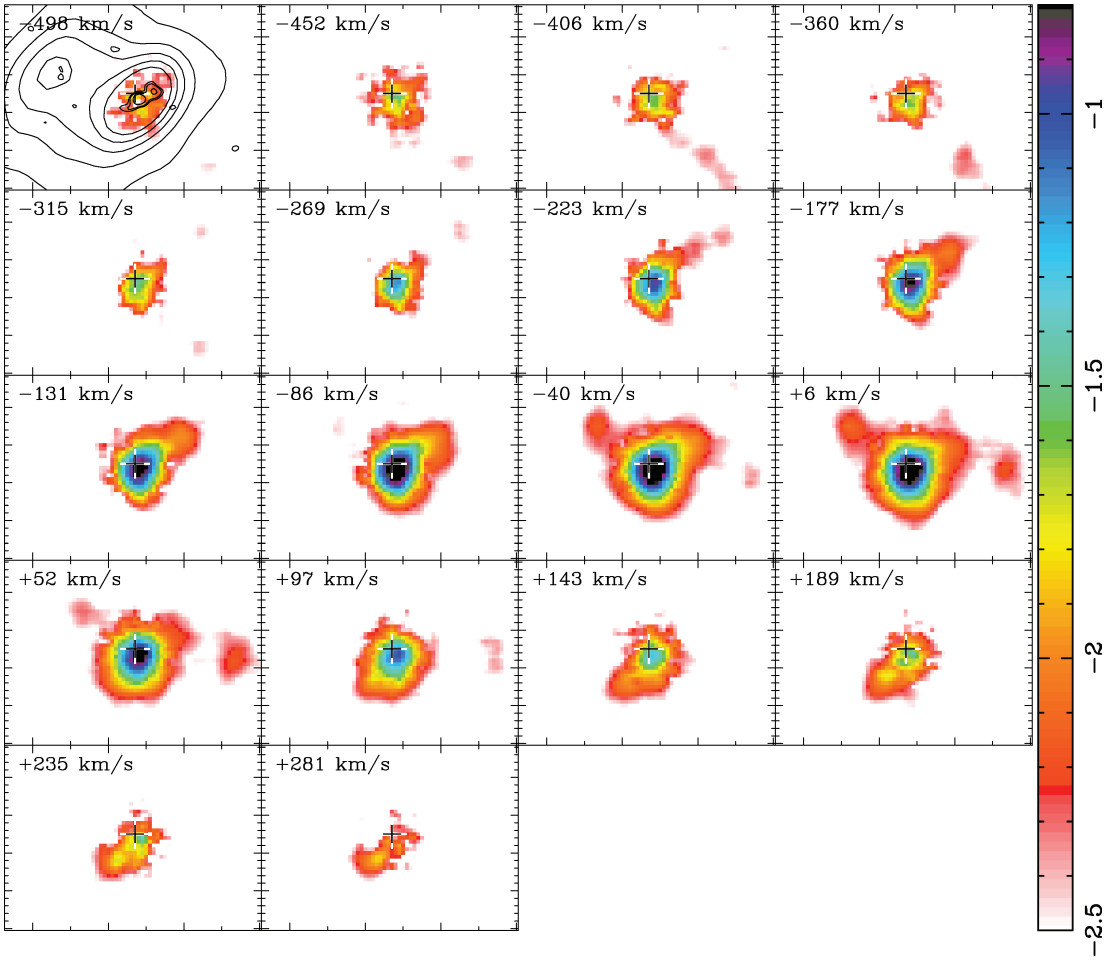

Figure 8. NGC 4051 velocity slices along the [S III] emission-line profile. The slices have a ∼46 km s^{-1} width and the central velocity is given in the upper-left hand corner. Radio contours, as in the previous figure, were overlaid on the upper-left hand map. The size of each slice field is 6.8 × 4.9 arcsec^2 and the tick marks in the *x*-axis are separated by 1 arcsec, as well as the large ones in the *y*-axis.

The only possible inflow was observed in the nucleus of NGC 2273, for which a redshift of up to 80 km s^{-1} is observed in the difference map V_R(Gas) − V_R(Stel) within ≈0.5 arcsec from the nucleus.

The [S III] radial velocity fields of NGC 4051 and 4941 do not show an obvious rotation pattern and are dominated by collimated outflows in the former and a milder less collimated outflow in the latter.

While the radial velocity maps show the velocity distribution of the gas with the strongest emission, the velocity channel maps show also the velocity distribution of gas with less intense emission.

For NGC 2273, the outflows can only be observed in the velocity channel maps, while the most intense emission comes from gas which mostly follow the velocity field of the stars. The presence of the outflows is supported by the increase in velocity dispersion at the corresponding locations. The fact that the outflow shows two kinematic components, and their apparent connection with two radio components observed in the 3.6 cm radio map suggest that the ejection of plasma by the active nucleus is not continuous, but occurs in a sequence of discrete components, resembling expanding 'bubbles'.

Emission in discrete components is observed also in the radial velocity maps of NGC 3227 and 3516, which show two blueshifted components in NGC 3227 and one in NGC 3516. These components have mean blueshifts of ≈ −200 km s^{-1} and are located at 1–2 arcsec from the nucleus, corresponding to projected distances at the galaxies of ≈100–200 pc.

In NGC 4593, there is also a small detached emission region at ≈1.3 arcsec from the nucleus (≈200 pc at the galaxy) with observed blueshifts larger than −50 km s^{-1}.

In the case of NGC 4051 the outflow is observed in what seems to be a projected conical structure, with blueshifts increasing from tens of km s^{-1} close to the nucleus up to −200 km s^{-1} at ≈2.3 arcsec, corresponding to a projected distance of ≈100 pc in the galaxy. A redshifted counterpart structure can also be observed. These apparently conical outflows seem to be continuous and not in discrete components as in the other galaxies discussed above.

Less conspicuous and collimated outflows – both blueshifted and redshifted and reaching velocities of up to 100 km s^{-1} seem to be present also in NGC 4941.

5.3 Variation of radial velocities with distance from the nucleus

The outflows observed in the radial velocity maps of NGC 3227, 3516 and 4051 show velocities which appear to increase with distance from the nucleus. This is unexpected, as, if the outflows are originated at the AGN, they should decelerate outwards, not

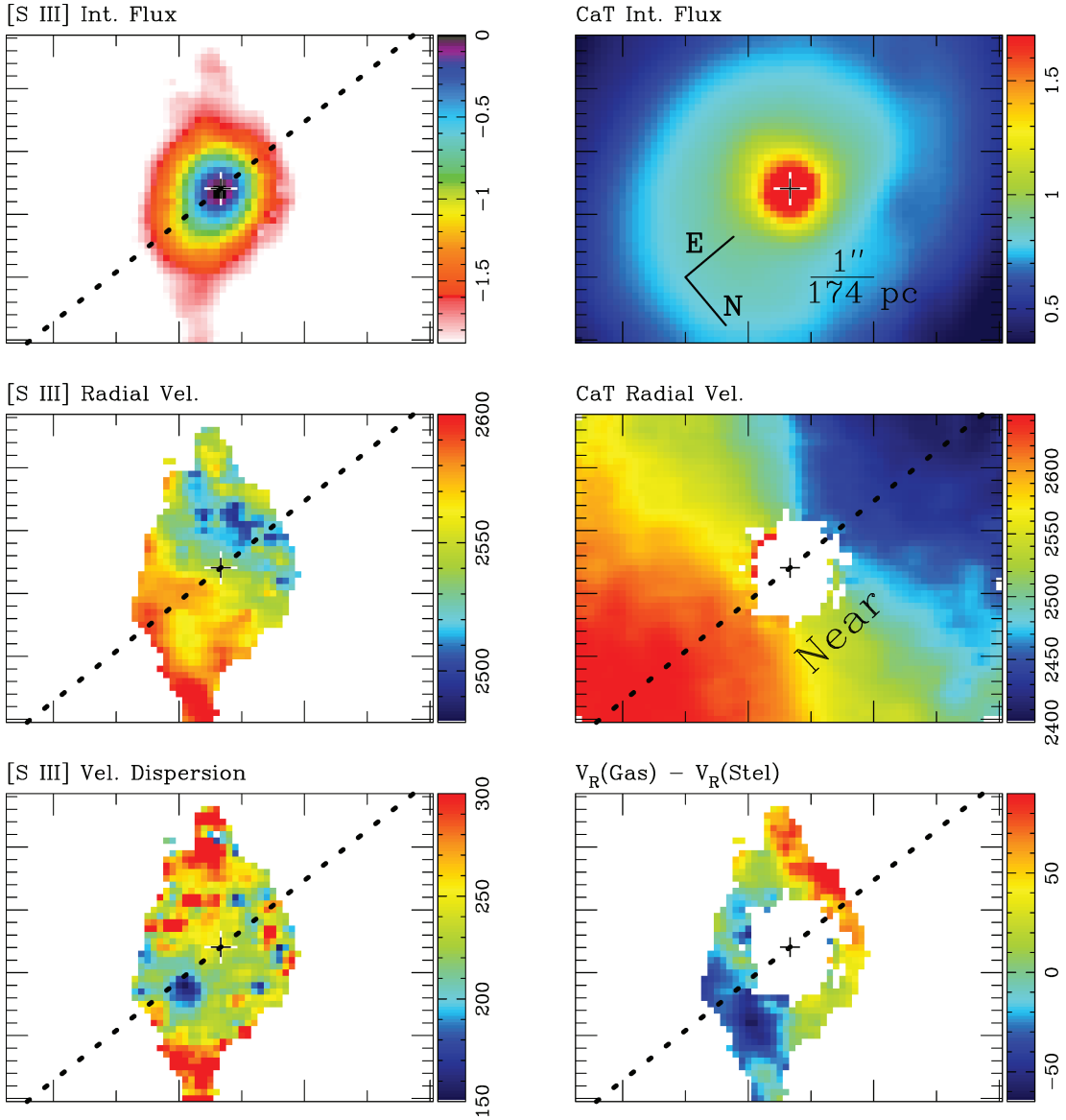

Figure 9. Gas kinematics of NGC 4593. Details are as described in the caption of Fig. 1 except that here we do not show radio contours. The systemic velocity for this galaxy is 2531 km s^{-1} (Barbosa et al. 2006).

accelerate. This puzzling result has also been observed previously in kinematic studies of the NLR of NGC 4151 and 1068 (Crenshaw et al. 2000; Das et al. 2005, 2006), leading the authors to propose acceleration mechanisms for the clouds leaving the nuclei.

The increase of velocity with distance from the nucleus is observed in the radial velocity maps of the galaxies above. Nevertheless, in the velocity slices of NGC 3227 and 4051 the highest velocities are observed close to the nuclei, with decreasing velocities being observed as the distance from the nucleus increases. Based on our NLR tomography we conclude that the gas leaving the nucleus is actually decelerating instead of accelerating. Deceleration seems also to be occurring in NGC 2273.

Why does this deceleration not appear in the radial velocity maps? The radial velocities are determined by the position of the peak of a given emission line. In an AGN spectrum, multiple gas components having different kinematics are added leading to a single emission-line profile, and the position of the line peak will depend on the relative intensity of each different component. As we extract the spectra closer to the nucleus, the emission from the gas in the galactic disc (which is dominated by rotation) may become the dominant component. As near the nucleus, this component has radial velocity close to zero, the result is a lower radial velocity as measured from the peak of the emission line. This effect can make a small nuclear outflow unnoticeable in the radial velocity map or make the outflow appear with a smaller velocity. On the other hand, in the velocity channel maps, the emission in the wings of the profiles is fully mapped, allowing the detection of gas with higher radial velocity, but with lower emission intensity. For NGC 3516 and other similar cases, where we detect detached components, our interpretation is that, since the outflows is not continuous, it can be also decelerating, and the velocity of the emission structure may have been higher when it was initially ejected from the nucleus.

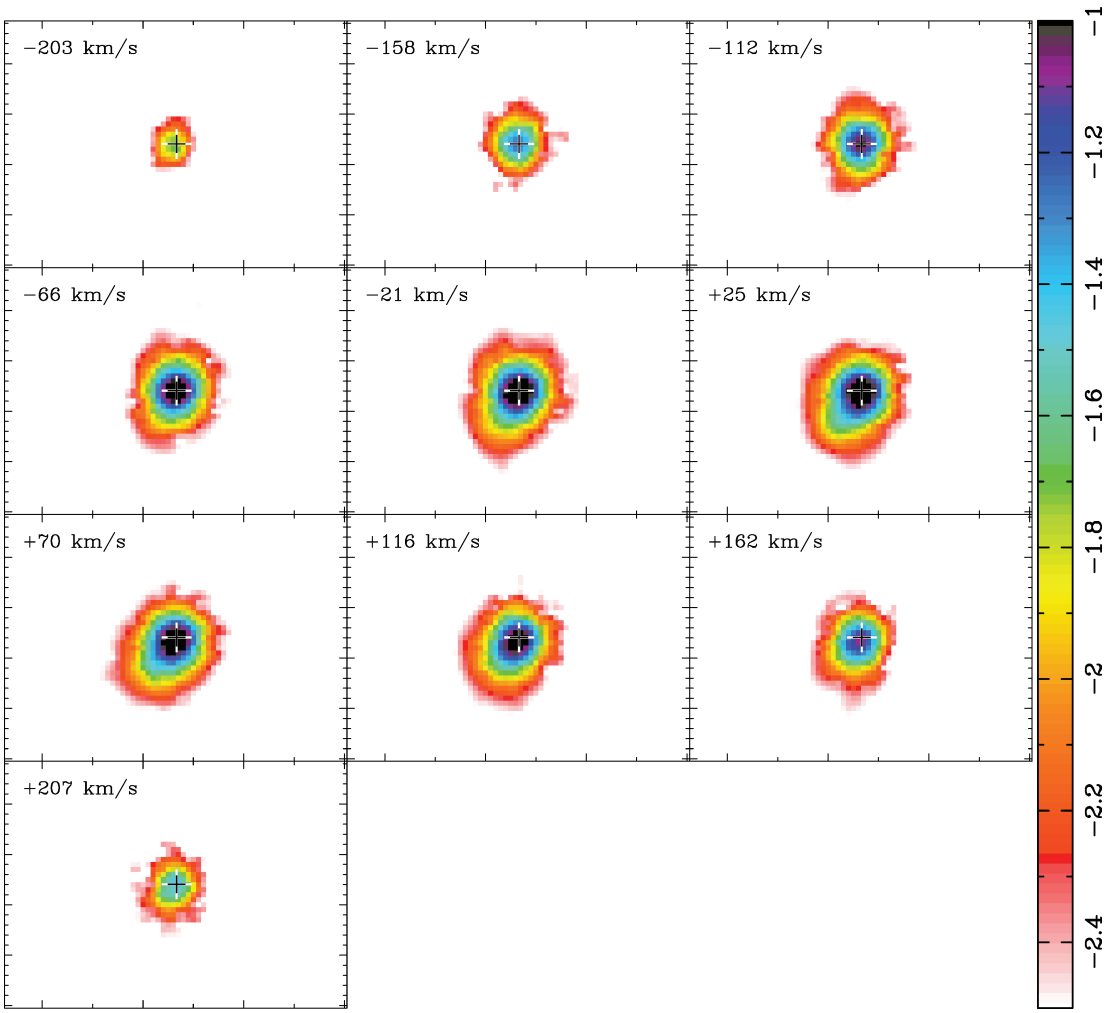

Figure 10. NGC 4593 velocity slices along the [S III] emission-line profile. The slices have a ∼46 km s^{-1} width and the central velocity is given in the upper-left hand corner. The size of each slice field is 6.8 × 4.9 arcsec^2 and the tick marks in the *x*-axis are separated by 1 arcsec, as well as the large ones in the *y*-axis.

5.4 Relation between the NLR kinematics and the radio ejecta

The outflows are observed in approximate alignment with the compact 3.6 cm radio structure for NGC 2273, 3227, 4051 and possibly also for NGC 4941. In the case of NGC 3516 the outflow seems to follow the 20 cm radio distribution. In NGC 4593 there is an outflowing cloud with low velocity dispersion which seems to be detached from the galaxy plane. In NGC 4941 there is suggestion of an additional outflow which seems to be unrelated to the compact radio emission.

The observed alignment between the outflowing components and the extended radio emission supports a physical association between the radio emission and the outflows, namely that the kinematics of the NLR is affected by the interaction of the radio plasma ejected by the AGN with the ISM of the host galaxy. The radio jet compresses the circumnuclear ISM, increasing its density and thus enhancing the emission of the gas which is photoionized by the nuclear source. The radio jet also deposits kinetic energy in the NLR, what is indicated by the increase in the gas velocity dispersion observed in the outflowing regions or in regions surrounding the outflows.

This result is in line with those of previous optical (e.g. Schmitt et al. 2003) and IR NLR studies which found good correlation between the NLR flux distributions and kinematics and radio emission in AGN (Riffel et al. 2006 using near infrared IFU observations, Blietz et al. 1994 using narrow band imaging, Forbes & Ward 1993; Veilleux, Goodrich & Hill 1997 using spectroscopy). Nevertheless, detailed studies at *HST* resolution of the NLR of some galaxies, like NGC 4151 (Kaiser et al. 2000) does not show clear correlation between the radio structure and the mass kinematics, suggesting that interaction with radio jets is not the only mechanism to produce NLR outflows.

In our galaxies we do not see a perfect spatial correlation between the radio image and the NLR outflows, only an alignment between them and signatures of interaction between the radio jet and the emitting gas in at least four galaxies. Thus we cannot discard the existence of other mechanisms contributing to the NLR outflows, such as accretion disc winds (Elvis 2000).

5.5 Mass outflow rates in the NLR

For the galaxies with detected outflows we have estimated lower limits to their mass outflow rate within the NLR ($\dot{M}$) through the equation:

$$\dot{M} = 2 n_{\rm e}\, m_{\rm p}\, A\, V_{\rm R}\, f, \qquad (1)$$

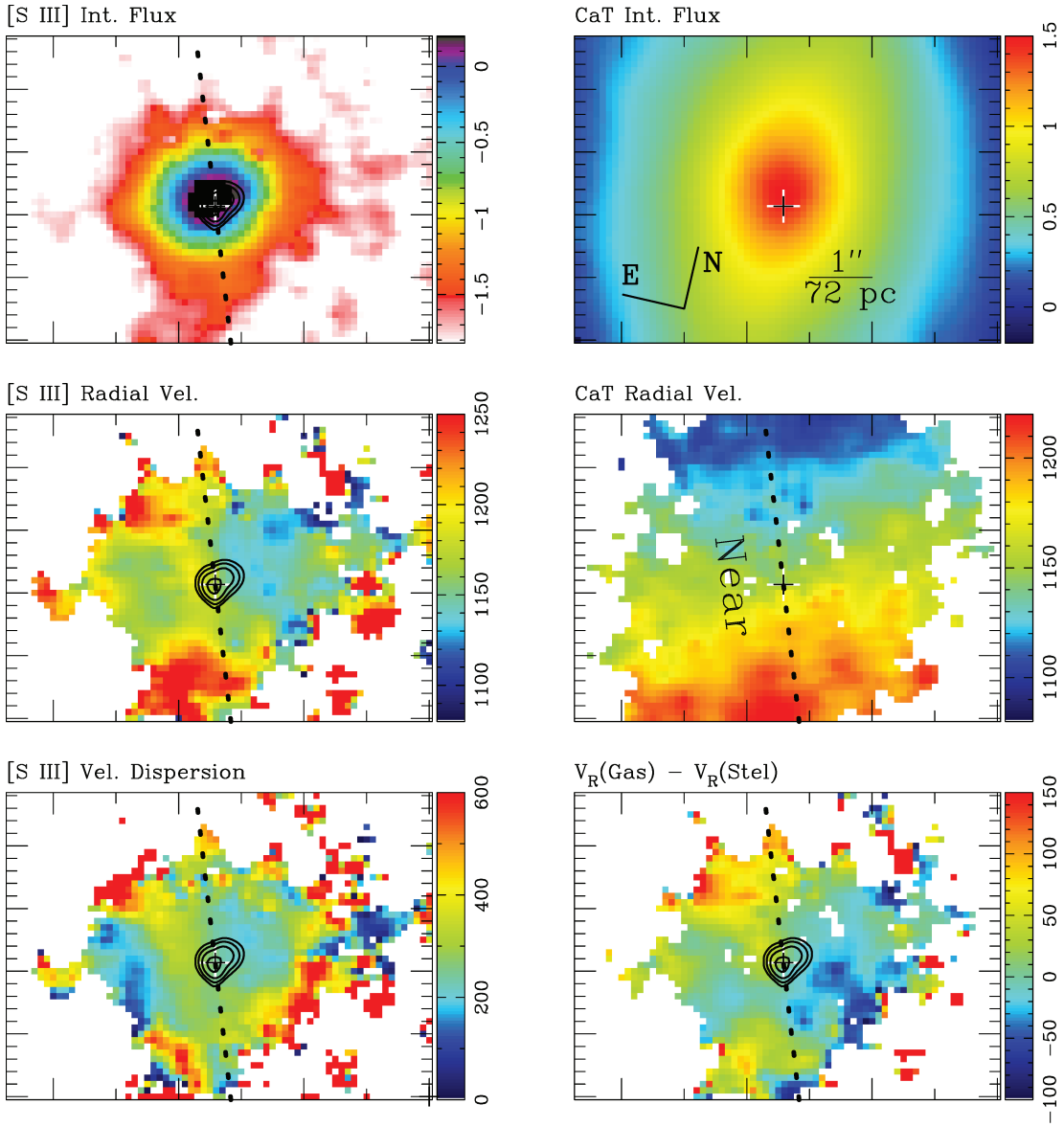

Figure 11. Gas kinematics of NGC 4941. Details are as described in the caption of Fig. 1 except that here we only show the contours of the radio 3.6 cm emission. The systemic velocity for this galaxy is 1161 km s^{-1} (Barbosa et al. 2006).

where m_p is the proton mass, n_e is the electronic density, A is the transverse area of the outflow, V_R is the average radial velocity of the outflow and f is the filling factor. The factor of 2 is introduced to take into account the likely presence of an undetected counter outflow. We assume that the outflow has a circular cross-section and then we determine the corresponding area A by measuring its projected diameter D directly in the radial velocity map or in the velocity channels maps. At the same location where we measure D we obtain the radial velocity V_R. The filling factor f is assumed to have a typical value of 10^{-3}. The electronic density n_e cannot be measured directly from our data so we assumed a typical value of $n_e = 10^2$ cm^{-3} and rewrite equation 1 with n_e in units of 10^2 cm^{-2} ($n_{e,100}$) as

$$\dot{M} = 0.2\, n_{e,100}\, m_p\, A\, V_R. \quad (2)$$

The radial velocities cannot be deprojected as the orientation of the outflow is unknown and therefore this calculation gives a lower limit to the mass outflow rate $\dot{M}$. These values, and those of the adopted D and V_R are listed in Table 3 for the outflows in the galaxies NGC 2273, 3227, 3516 and 4051 (for which these parameters are measurable). For NGC 4051 we could observe also the counter outflow, instead of using the factor 2 in equation 1, we summed the $\dot{M}$ of both outflows.

The obtained $\dot{M}$ values range from 1 to $\approx$50 $\times$ $n_{e,100}$ 10^{-3} M$_\odot$ yr^{-1}, which can be compared with those reported in the literature. Crenshaw & Kraemer (2007) obtain $\dot{M} \approx 0.16$ M$_\odot$ yr^{-1} for NGC 4151 using blueshifted absorption lines in the UV spectrum of NGC 4151. Veilleux, Cecil & Bland-Hawthorn (2005) report values of $\dot{M}$ calculated from the warm ionized gas masses in the NLR and ENLR of 10^5–10^7 M$_\odot$ (reported to be accurate within 0.5 dex due to uncertainties in the filling factor) and dynamical times of 10^5–10^6 yr. The result is $\dot{M}$ in the range $\sim$0.1 to 10 M$_\odot$ yr^{-1}. These values are a factor of 10–100 higher than ours, what is probably due to the fact that the objects in our sample are less luminous than those studied by Veilleux et al. (2005).

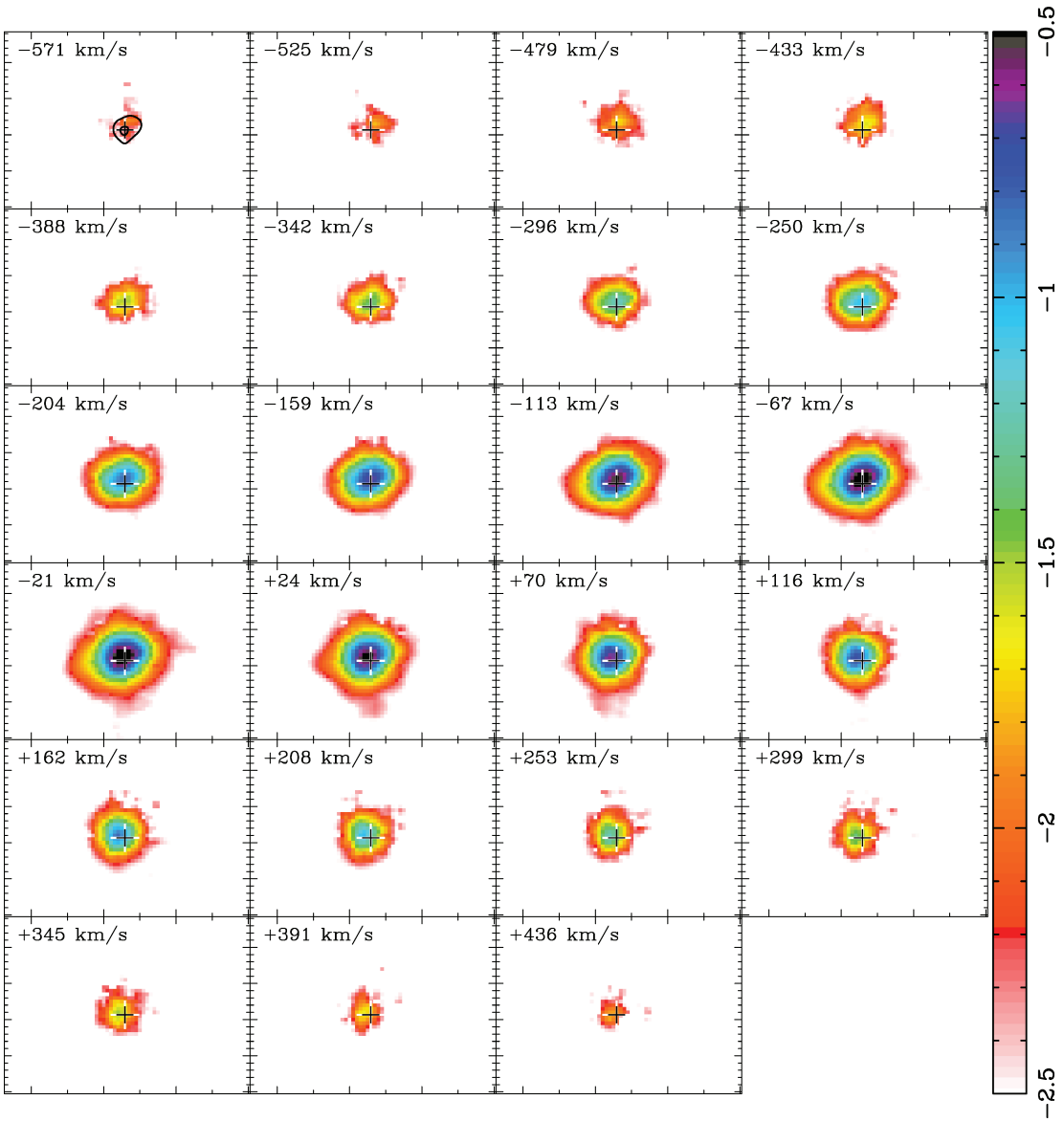

Figure 12. NGC 4941 velocity slices along the [S III] emission-line profile. The slices have a ∼46 km s^{-1} width and the central velocity is given in the upper-left hand corner. Radio contours, as in the previous figure, were overlaid on the upper-left hand map. The size of each slice field is 6.8 × 4.9 arcsec^2 and the tick marks in the *x*-axis are separated by 1 arcsec, as well as the large ones in the *y*-axis.

Table 3. Mass outflow rate $\dot{M}$, diameter D of the outflow cross-section area and radial velocities V_R for the observed outflows.

Galaxy	Outflow location	D (pc)	$\lvert V_R \rvert$ (km s^{-1})	$\dot{M}$ ($\times n_{e,100}\ 10^{-3}$ M$_\odot$ yr^{-1})
NGC 2273	W ≤ 1 arcsec	110.6	400	19.4
NGC 2273	W ∼1.5 arcsec	136.8	160	11.8
NGC 3227	N	148.6	180	15.8
NGC 3516	N	220.4	265	51
NGC 4051	E	45.0	170	0.7
NGC 4051	W	44.5	120	0.5

Notes. Column (1): galaxy identification; column (2) identification of the outflow with orientation and extent listed when necessary; column (3): D; column (4): V_R; column (5): $\dot{M}$.

We can also compare the $\dot{M}$ values with the mass accretion rate $\dot{M}_{acc}$ necessary to feed the supermassive black hole in the nuclei of the galaxies of our sample. We have calculated the accretion rate using:

$$\dot{M}_{acc} = \frac{L_{bol}}{\eta c^2}, \quad (3)$$

where L_{bol} is the bolometric luminosity, η is the efficiency factor for conversion of accreted mass into radiation, assumed to be 0.1 – the typical value for thin accretion discs (Frank, King & Raine 2002), and $L_{bol} \approx 20\, L_{X,(2-10\,keV)}$ (Elvis et al. 1994). We have obtained the X-ray fluxes from the work of Panessa et al. (2006) for NGC 2273, 3227, 3516 and 4051. The values derived for L_{bol} and the resulting mass accretion rates are listed in Table 4 together with the resulting mass accretion rates. In the fourth column we list the mass outflow rates, for comparison. It can be seen that the mass outflow rates for NGC 3227, 3516 and 4051 are, respectively, 21.6, 12.4 and 10.9

Table 4. Accretion rate $\dot{m}_{\rm acc}$ compared to the mass outflow rate $\dot{M}$.

Galaxy	$L_{\rm bol}$ (10^{41} erg s^{-1})	$\dot{M}_{\rm acc}$ ($\times 10^{-3}$ M$_\odot$ yr^{-1})	$\dot{M}$ ($\times n_{\rm e,100}\, 10^{-3}$ M$_\odot$ yr^{-1})	$P_{\rm out}$ (10^{41} erg s^{-1})
NGC 2273	10.14	0.09	31.2[a]	0.044[a]
NGC 3227	82.4	0.73	15.8	0.0068
NGC 3516	459.8	4.1	51.0	0.048
NGC 4051	13	0.11	1.2[a]	0.00034[a]

[a]Sum of two outflow components.

times the mass accretion rate. In the case of NGC 2273, this ratio is 363, but Panessa et al. (2006) point out that this galaxy is Compton thick in X-rays and estimate that the actual emitted flux is 57 times larger than observed. Using the corresponding luminosity to this higher flux, the ratio between the mass outflow and mass accretion rates in this galaxy decreases to 6.4.

We thus conclude that, on average, there is ∼10–20 times more mass outflowing from the nuclear region than being accreted into the black hole. Veilleux et al. (2005) report similar ratio between mass outflow rates and nuclear accretion rates in AGN, even considering that the AGN in their sample are much more luminous than the ones studied in this work. A larger outflow rate can be understood if the outflowing gas does not originate in the nucleus, but is actually gas from the circumnuclear ISM being pushed away by a nuclear jet or wind.

We can also compare the power in the outflow $P_{\rm out}$ to the luminosity of the AGN $L_{\rm bol}$. The kinetic power was calculated as $P_{\rm out} = 1/2\, \dot{M}\, V_{\rm R}^2$, where $V_{\rm R}$ is the adopted outflow velocity. These values are listed in the last column of Table 4. The resulting powers in the outflow are in the range $10^{-5} < P_{\rm out}/L_{\rm bol} < 10^{-4}$, thus negligible when compared to the accretion power.

As we have concluded that the outflows are, in most cases, related to the radio jet, we now consider the assumption that the observed outflows are generated by a nuclear radio jet pushing the circumnuclear ISM of the galaxy. Under this assumption we can estimate a lower limit for the mass ejection rate in the radio jet $\dot{M}_{\rm jet}$ if we consider that the jet is relativistic as it leaves the AGN and its kinetic energy has been transferred to the NLR outflow with an efficiency $\eta_{\rm jet}$:

$$P_{\rm jet} \approx \eta_{\rm jet}(\gamma - 1)\, \dot{M}_{\rm jet}\, c^2 = P_{\rm out} \quad (4)$$

where γ is the Lorentz factor. A value of $\gamma = 6$ was obtained by Biretta, Sparks & Macchetto (1999) for M 87. If this is a typical value, and $\eta_{\rm jet} \approx 0.5$, then we obtain, for $10^{-5} L_{\rm bol} < P_{\rm out} < 10^{-4} L_{\rm bol}$, and $L_{\rm bol} = 0.1\, \dot{M}_{\rm acc}\, c^2$, a lower limit for $\dot{M}_{\rm jet}$ in the range $10^{-6} \dot{M}_{\rm acc} < \dot{M}_{\rm jet} < 10^{-5} \dot{M}_{\rm acc}$. It may be that the Lorentz factor is overestimated as it appears that the jets in Seyferts are predominantly sub-relativistic (Whittle et al. 2004) but this uncertainty does not affect the order of magnitude of the above estimate.

6 SUMMARY AND CONCLUSIONS

We have mapped the [S III] λ9069 emitting gas kinematics of 6 Seyfert galaxies using 2D GMOS-IFU observations of the circumnuclear region (≈5 × 7 arcsec^2), corresponding to the inner few hundred parsecs at a spatial resolution ranging from 20 to 180 pc. We derived emission-line flux distributions, radial velocity and velocity dispersion maps along the NLR, as well as velocity channel maps (velocity tomography) in the [S III] emission line. The main results of this paper are as follows.

(i) The emission-line flux distributions are always extended to more than ≈200 pc from the nucleus.

(ii) The gas kinematics is dominated by circular rotation in the galaxy disc, similarly to the stellar kinematics studied in Paper I. But, in all cases we find also additional outflowing components, revealed by the subtraction of the stellar rotation component.

(iii) Gas emission is not always restricted to the outflow region, being spread over most of the IFU field. The gas which is not outflowing has a similar kinematics to the stars which are rotating in the galactic plane, suggesting that it is located also in the plane.

(iv) The outflows show radial velocities in the range 100–400 km s^{-1}, and are usually collimated in spatial association with elongated radio emission at 3.6 cm and/or 20 cm, indicating a connection between the radio emission and the NLR gas emission. Some of the observed outflows are not continuous, showing discrete spatial components.

(v) The outflows are oriented at random angles relative to the galaxy major axis, indicating that they leave the galactic plane at angles smaller than 90°. The majority of the outflows are projected against the far side of the galaxy.

(vi) While the radial velocity maps suggest that the radial velocity usually increases with distance from the nucleus, the velocity tomography shows that, for at least half of our sample, the highest velocities are observed close to the nucleus, suggesting deceleration of the NLR clouds. This difference may be attributed to the lower flux in the highest radial velocity emission components relative to that in the low velocity components close to the nucleus.

(vii) We have obtained gas mass outflow rates in the range 1 to ≈ 50 × 10^{-3} M$_\odot$ yr^{-1} which are ≈10–20 times the accretion rate necessary to feed the AGN. Similar ratios have been obtained in previous works for AGN in general, and indicate that the outflowing NLR gas does not originate from in the active nucleus, but is the circumnuclear ISM of the host galaxy being pushed away by a nuclear radio jet or outflow.

(viii) The kinetic power of the outflow is 4–5 orders of magnitude smaller than the AGN luminosity. Assuming kinetic energy transfer between the radio jet and the NLR outflows, we estimate that the mass ejection rate in the radio jet is 5–6 orders of magnitude smaller than the mass accretion rate to feed the nuclear supermassive black hole.

ACKNOWLEDGMENTS

We acknowledge support from the Brazilian funding agencies CNPq and CAPES. Basic research at the US Naval Research Laboratory is supported by the Office of Naval Research.

The author is very grateful to Dr Roberto Maiolino, Dr Alessandro Marconi and the Arcetri group for the hospitality given during his permanence at the Observatory of Arcetri where part of this work was developed.

We thank the referee for the valuable suggestions which helped to improve the paper.

Based on observations obtained at the Gemini Observatory, which is operated by the Association of Universities for Research in Astronomy, Inc., under a cooperative agreement with the NSF on behalf of the Gemini partnership: the National Science Foundation (United States), the Science and Technology Facilities Council (United Kingdom), the National Research Council (Canada), CONICYT (Chile), the Australian Research Council (Australia), Ministrio da Cincia e Tecnologia (Brazil) and SECYT (Argentina). Observing programmes GN-2002B-Q-15, GN-2003A-Q-20 and GN-2004A-Q-1.

REFERENCES

Allington-Smith J. et al., 2002, PASP, 114, 892
Barbosa F. K. B., Storchi-Bergmann T., Cid Fernandes R., Winge C., Schmitt H., 2006, MNRAS, 371, 170 (Paper I)
Biretta J. A., Sparks W. B., Macchetto F., 1999, ApJ, 520, 621
Blietz M., Cameron M., Drapatz S., Genzel R., Krabbe A., van der Werf P., Sternberg A., Ward M., 1994, ApJ, 421, 92
Capetti A., Axon D. J., Macchetto F., Sparks W. B., Boksenberg A., 1996, ApJ, 469, 554
Cooke A. J., Baldwin J. A., Ferland G. J., Netzer H., Wilson A. S., 2000, ApJS, 129, 517
Crenshaw D. M., Kraemer S. B., 2007, ApJ, 659, 250
Crenshaw D. M. et al., 2000, AJ, 120, 1731
Das V., Crenshaw D. M., Kraemer S. B., Deo R. P., 2006, AJ, 132, 620
Das V. et al., 2005, AJ, 130, 945
Dumas G., Mundell C. G., Emsellem E., Nagar N. M., 2007, MNRAS, 379, 1249
Elvis M., 2000, ApJ, 545, 63
Elvis M. et al., 1994, ApJS, 95, 1
Erwin P., Sparke L. S., 2003, ApJS, 146, 299
Falcke H., Wilson A. S., Simpson C., 1998, ApJ, 502, 199
Ferruit P., Wilson A. S., Mulchaey J., 2000, ApJS, 128, 139
Forbes D. A., Ward M. J., 1993, ApJ, 416, 150
Frank J., King A., Raine D., 2002, Accretion Power in Astrophysics. Cambridge Univ. Press, Cambridge
Fraquelli H. A., Storchi-Bergmann T., Binette L., 2000, ApJ, 532, 867
Fraquelli H. A., Storchi-Bergmann T., Levenson N. A., 2003, MNRAS, 341, 449
González Delgado R. M., Arribas S., Pérez E., Heckman T., 2002, ApJ, 579, 188
Kaiser M. E. et al., 2000, ApJ, 528, 260
Miyaji T., Wilson A. S., Perez-Fournon I., 1992, ApJ, 385, 137
Mulchaey J. S., Tsvetanov Z., Wilson A. S., Perez-Fournon I., 1992, ApJ, 394, 91
Mundell C. G., Wrobel J. M., Pedlar A., Gallimore J. F., 2003, ApJ, 583, 192
Nagar N. M., Wilson A. S., Mulchaey J. S., Gallimore J. F., 1999, ApJS, 120, 209
Nelson C. H., Weistrop D., Hutchings J. B., Crenshaw D. M., Gull T. R., Kaiser M. E., Kraemer S. B., Lindler D., 2000, ApJ, 531, 257
Panessa F., Bassani L., Cappi M., Dadina M., Barcons X., Carrera F. J., Ho L. C., Iwasawa K., 2006, A&A, 455, 173
Riffel R. A., Storchi-Bergmann T., Winge C., Barbosa F. K. B., 2006, MNRAS, 373, 2
Riffel R. A., Storchi-Bergmann T., Winge C., McGregor P. J., Beck T., Schmitt H., 2008, MNRAS, 385, 1129
Ruiz J. R., Crenshaw D. M., Kraemer S. B., Bower G. A., Gull T. R., Hutchings J. B., Kaiser M. E., Weistrop D., 2001, AJ, 122, 2961
Ruiz J. R., Crenshaw D. M., Kraemer S. B., Bower G. A., Gull T. R., Hutchings J. B., Kaiser M. E., Weistrop D., 2005, AJ, 129, 73
Schmitt H. R., Kinney A. L., 1996, ApJ, 463, 498
Schmitt H. R., Ulvestad J. S., Antonucci R. R. J., Kinney A. L., 2001, ApJS, 132, 199
Schmitt H. R., Donley J. L., Antonucci R. R. J., Hutchings J. B., Kinney A. L., 2003, ApJS, 148, 327
Storchi-Bergmann T., Wiklson A. S., Baldwin J. A., 1992, ApJ, 396, 45
Storchi-Bergmann T., Winge C., Ward M. J., Wilson A. S., 1999, MNRAS, 304, 35
Veilleux S., Goodrich R. W., Hill G. J., 1997, ApJ, 477, 631
Veilleux S., Shopbell P. L., Rupke D. S., Bland-Hawthorn J., Cecil G., 2003, AJ, 126, 2185
Veilleux S., Cecil G., Bland-Hawthorn J., 2005, ARA&A, 43, 769
Wilson A. S., Tsvetanov Z. I., 1994, AJ, 107, 1227
Whittle M., 1992, ApJS, 79, 49
Whittle M., Silverman J. D., Rosario D. J., Wilson A. S., Nelson C. H., 2004, in Storchi-Bergmann T., Ho, L. C., Schmitt, Henrique R., eds, Proc. IAU Symp. 222, The Interplay Among Black Holes, Stars and ISM in Galactic Nuclei. Cambridge Univ. Press, Cambridge, p. 299

This paper has been typeset from a TEX/LATEX file prepared by the author.